Diffusive transport of adsorbed n-alkanes along e-beam irradiated plane surfaces and nanopillars

Gleb S. Zhdanov[1], *Maksim S. Lozhkin*[1]

[1]St. Petersburg State University, Department of Physics, Russia

Corresponding author: Gleb S. Zhdanov, St. Petersburg State University, Department of Physics, Russia, e-mail: gszhdanov@mail.ru

Abstract

Diffusion of adsorbed n-alkanes was studied by means of electron beam induced deposition (EBID) technique. Carbon ring-like and pillar-like deposits were produced on bulk and thin substrates in a scanning electron microscope (SEM) operated in a "spot" mode. Residual n-alkanes used as a precursor gas were delivered to the beam interaction region (BIR) via surface diffusion.

The model of adsorbate diffusion along a heterogeneous surface with different diffusion coefficients D_1 and D_2 outside and inside the BIR, respectively, was proposed to explain the measured deposition rates. The estimates for diffusion coefficients ranging from ~$1x10^{-10}$ to ~$1x10^{-7}$ cm^2s^{-1} at room temperature on surfaces with different roughness were obtained. These estimates most likely should be attributed to n-decane molecules expected to play the key role in the deposition process. Clusters of polymerized molecules produced by irradiation were assumed to act as effective traps hampering surface diffusion. For high D_1/D_2 ratios the deposition rates were found to be practically independent of the substrate material and initial roughness.

Keywords: electron beam induced deposition, specimen contamination, carbon nanostuctures, n-alkane surface diffusion, diffusion over rough surfaces

1. Introduction

The interaction of fast electrons with organic molecules has been of interest from the early days of electron microscopy. Prolonged irradiation caused image deterioration resulting from electron-beam-induced contamination of the specimen surface. In the first attempts to explain this phenomenon [1], organic molecules impinged on the irradiated surface directly from the gas phase were assumed to be responsible for specimen contamination. Later [2, 3], the surface diffusion of adsorbed molecules driven by the density gradient was proposed as the major transport mechanism. This hypothesis explained high contamination rates, which grew with decreasing beam radius R approximately as R^{-2} [3].

The renewed interest to the contamination problem in the 1990s was caused by progress in a versatile technique often denoted by an acronym EBID (electron-beam-induced deposition) [4].

Electron beams focused to a spot of about 1nm diameter were used to produce nanoscale features on substrates by cracking adsorbed precursor molecules into volatile and nonvolatile fragments. Carbon is one of the most often used deposit materials while residual n-alkanes (C_NH_{2N+2}) are often used as a precursor. EBID of carbon has numerous applications including fabrication and repair of lithography masks, fabrication of supertips for probe microscopes, "soldering" of nanofibers, etc. [4].

Using EBID for nanoscale patterning of macroscopic substrates requires high deposition rates. These may depend on the diffusivities of molecules impinged on the substrate and on the deposit. There is a large amount of data concerning adsorption and diffusion of n-alkanes under well defined conditions in ultrahigh vacuum (UHV), but most results were obtained with metal single crystals used as substrates (e.g., [5,6]) Quantitative understanding of the behavior of n-alkanes under both UHV and non-UHV conditions on most substrates of largest technological interest is still lacking.

The potentials of EBID as a technique complimentary to conventional methods of adsorbate characterization have been recently recognized [4, 7-9]. One of the advantages of this technique is that it allows a large number of precursor/substrate pairs to be studied, but complications arise due to the simultaneous presence of several molecular species including undesired contaminants. As stated in the review [10], "published values of diffusion coefficients, residence times and cross sections determined from focused electron beam experiments are very limited and show a large scatter".

In this work we study the effect of the substrate material and roughness on the diffusivities of n-alkane adsorbates under common conditions of EBID experiments usually performed at 10^{-6} – 10^{-7} Torr total residual pressure. EBID of carbon was carried out and monitored in a scanning electron microscope (SEM). Residual n-alkanes were used as a precursor. The deposits having ring-like and pillar-like shapes were produced on a number of thin and bulk substrates. The pillar vertical growth rates as high as $3x10^2$ nm/s were measured indicating that delivery of molecules to the beam interaction region (BIR) occurred via surface diffusion . Direct impingement of molecules onto the pillar from the gas phase would give growth rates, smaller by several orders of magnitude .

The theory [3] of specimen contamination produced by a focused electron beam was extended to include the possibility of different diffusion conditions for hydrocarbon molecules on the substrate and on the deposit. In contrast to theoretical predictions and common EBID models based on the assumption of a constant diffusion coefficient, we observed an increase of the volumetric growth rate of deposited features with decreasing BIR radius. To explain this discrepancy we suggested that the irradiated surface should be characterized by two different diffusion coefficients D_1 and D_2 outside and inside of the irradiated area, respectively. The ratio D_1/D_2 for ring-like deposits formed on smooth surfaces was estimated to be as high as ~10^3.

The effect of surface contamination on the deposition rate revealed itself on freshly cleaved graphite crystals starting from less than 0.1 ML coverage. Clusters of cracked and polymerized precursor molecules produced on smooth surfaces by irradiation behaved as local traps hampering surface diffusion. Much smaller effect was observed on substrates covered by discontinuous gold films containing numerous cracks and pits with depths of several dozen nanometers. Molecules seem to easily overcome large but rarely located obstacles by moving around or across them.

While the diffusion flow is directed towards the beam incidence point, some molecules performing random walk move from the BIR in the opposite direction and further desorb from the surface. The fraction of desorbed molecules compared to that of polymerized ones increases

with the ratio D_1/D_2 producing the same effect as might be caused by a semi-transparent reflective wall at the BIR border. This effect slows down the deposition rate and should be accounted for in theoretical EBID models considering surface diffusion.

Among various n-alkanes present in the specimen chamber only one or two species most likely determine the rate of electron beam induced reactions. We suggest n-decane as the key participant in the deposition process.

2. Physical model

We consider an irradiated surface in equilibrium with the gas phase. Molecules arriving at a rate J_{vap} (molecules/cm^2 s*)* either return back to the vacuum after spending an average time τ_a in physisorbed state or are dissociated and pinned to the surface during a time τ_j.

The rate equation based on the mass conservation law can be written as [10]

$$\frac{\partial n}{\partial t} = s(1-\frac{n}{n_0})J_{vap} + J_{diff} - \frac{n}{\tau_a} - \frac{n}{\tau_j} \qquad (1)$$

where n is the density of adsorbed molecules, s is the sticking coefficient, n_0 is the quantity approximately equal to the reciprocal of the area occupied by a molecule, and J_{diff} is the flux of molecules delivered by surface diffusion to the unit area per unit time. The term in brackets accounts for a limited surface area available for Langmuir-type adsorption. The time τ_j is inversely proportional to the current density J of electrons participating in dissociation reactions

$$\tau_j = \frac{e}{\sigma J} \qquad (2)$$

where σ is the dissociation cross section, and e is the electron charge..

For planar deposits the term n/τ_j multiplied by a volume Ω of a molecule determines the vertical growth rate

$$\frac{dh}{dt} = \frac{n}{\tau_j}\Omega \qquad (3)$$

The average value of this quantity multiplied by the area S of the deposit gives the volumetric growth rate

$$\frac{dV}{dt} = <\frac{dh}{dt}> S = \frac{dN_{dep}}{dt}\Omega \qquad (4)$$

where dN_{dep}/dt is the number of molecules deposited per unit time. Both dh/dt and dV/dt can be determined by analysis of subsequent SEM and AFM images obtained at various stages of the deposition process. Typically, dV/dt and hence n/τ_j do not change considerably with time. For any system the time step Δt can be found during which n and other variables in Eq.(1) can be considered as time independent. Under these assumptions the mass balance equation for the system with circular symmetry takes the form

$$s(1-\frac{n}{n_0})J_{vap} + D(\frac{d^2n}{dr^2} + \frac{1}{r}\frac{dn}{dr}) - \frac{n}{\tau_a} - \frac{n}{\tau_j} = 0 \qquad (5)$$

where r is the radial distance from the beam incidence point, and D is the surface diffusion coefficient which is assumed to be constant, just as the residence time τ_a. In the following for simplicity we will assume s =1.

The quasi-steady state rate equation forms a basis of the continuum model often used for the interpretation of EBID experiments [9, 10]. To find an analytical solution, additional restrictions on the dissociation time τ_j and the current density J should be imposed. With τ_j = const, Eq.(5) can be reduced to one of the type of Bessel equations. Setting $J=J_0 = const$ for $r < R$ and $J = 0$ for $r > R$ gives two different solutions for the densities n_1 and n_2 outside and inside of the uniformly irradiated area of radius R, respectively. These solutions are then sewed together using concentration and flux continuity at the boundary.

The first strict solution was obtained by Muller [3] for the case $n << n_0$ and D = const. We extended and modified his approach in Appendix A to consider the more general case of different diffusion conditions on the substrate and the deposit. The net diffusion flow across the border determined by Eq.(A9) which is a direct consequence of Fick's first law, can be written as a difference of two terms

$$L = 2\pi R D_1 \frac{dn_1}{dr}(r = R) = 2\pi D(n_\infty - n_R)(R/\lambda_1)\frac{K_1(R/\lambda_1)}{K_0(R/\lambda_1)} \equiv L^+ - L^- \qquad (6)$$

where L^+ is the arrival rate of molecules to the irradiated area by surface diffusion followed by their dissociation, L^- is the sink rate of molecules from the irradiated area by diffusion, n_∞ and n_R are the densities at $r \to \infty$ and $r = R$, respectively, D_1 and λ_1 are the diffusion coefficient and diffusion length of molecules on the unexposed surface, $K_0(R/\lambda_1)$ and $K_1(R/\lambda_1)$ are the modified Bessel functions of the second kind. Surface diffusion is the dominant material supply mechanism when $\lambda_1 >> R$. Then, using asymptotics of the Bessel functions: $K_0(x) \approx \ln(1.13/x)$, $K_1(x) \approx 1/x$ for $x << 1$ [11], we can rearrange Eqs. (6), (A5)-(A8) as follows

$$L^+ = 2\pi D_1 p n_\infty \qquad (7)$$

$$L^- = \frac{L^+}{1 + qD_2/D_1} \qquad (8)$$

$$L = \frac{L^+}{1 + D_1/qD_2} \qquad (9)$$

$$n_R = \frac{n_\infty}{1 + qD_2/D_1} \qquad (10)$$

with

$$p = \frac{R}{\lambda_1}\frac{K_1(R/\lambda_1)}{K_0(R/\lambda_1)} \approx \left[\ln(1.13\lambda_1/R\right]^{-1} \qquad (11)$$

$$q \approx \frac{1}{p}\frac{R}{\lambda_2}\frac{I_1(R/\lambda_2)}{I_0(R/\lambda_2)} \qquad (12)$$

Here $I_0(R/\lambda_1)$, $I_1(R/\lambda_1)$ are the modified Bessel functions of the first kind.

In most practical cases, J drops off with increasing distance r from the beam incidence point approximately as a Gaussian, making the choice of the edge radius R rather ambiguous. Due to the logarithmic dependence of the left-hand side terms in Eqs. (7)-(12) on the ratio λ_1/R, the accuracy of determination of both λ_1 and R within reasonable limits is of minor importance. We took $R = r_2$ for ring-like deposits with the outer radius r_2 and $R = r_{base.}$ for pillars with the base radius r_{base}. From the published data [12, 13] and our estimates, λ_1 on various substrates most likely ranges from about 10 μm to 30 μm at room temperature. The values of R for specimens used in this work ranged from 2.7 μm to 4.1 μm for ring-like deposits and from 30 nm to 100 nm for pillars. Taking the mean values and setting λ_1 =20 μm, R_{ring} = 3.5 μm, $R_{pilla\ r}$ = 50 nm yields

$$p_{ring} \approx 0.6, \qquad p_{pillar} \approx 0.16, \qquad w \equiv p_{ring}/p_{pillar} \approx 3.5 \tag{13}$$

Our experiments were performed with beam currents large enough to decompose all incoming molecules. Indeed, tenfold current increase did not cause any remarkable increase in deposition rate. Under these conditions, the beam profile affects the deposit geometry rather than the deposition rate leaving considerable freedom for the choice of λ_2 in Eq. (12). It is reasonable to assume the average value $<\lambda_2>$ equal to about half the penetration length of diffusing molecules into the BIR. Hence, for rings of the width $\Delta r \approx R/3$ we can take $<\lambda_2> = \Delta r/2 \approx R/6$. As shown in Appendix B, diffusion along a conical pillar with a base radius $r_{base} = R$ obeys the same equation as that for the plane surface with $<\lambda_2> = <r/2> \approx R/4$. The ratio of modified Bessel functions $I_1(x)/I_0(x)$ in Eq. (12) closely approaches unity for $x \geq 3$. Replacing λ_2 by $<\lambda_2>$ in Eq. (12), yields $q \approx 10 \pm 2$ for both pillars and rings. For the case D = const any choice of $q > 4$ would give less than 20% correction to the value of the diffusion flow L in Eq.(9). In the following we assume $q = 10$ independent of the deposit shape

Setting the deposition rate approximately equal to the rate of their delivery via surface diffusion gives

$$\frac{dN_{dep}}{dt} \approx L = \frac{2\pi D_1 p n_\infty}{1 + D_1 / qD_2} \tag{14}$$

The saturation density n_∞ in Eq. (14) can be determined from the equilibrium condition on the unexposed surface (without diffusion and dissociation terms and with $s = 1$ in Eq.(5)) as follows

$$n_\infty = J_{vap}\left(\frac{J_{vap}}{n_0} + \frac{1}{\tau_a}\right)^{-1} \tag{15}$$

When several n-alkanes are present in the residual atmosphere their contributions to the total deposition rate are determined by the product $D_1 n_\infty$ in Eq. (14) and vary with the number N of carbon atoms in a chain. For a mixture of molecular species with comparable concentrations in the gas phase, the partial saturation densities n_∞ increase with τ_a. To relate the diffusion coefficient with τ_a we use Arrhenius expressions

$$D = D_0 \exp(-E_d/RT), \qquad \tau_a = \tau_0 \exp(E_a/RT) \tag{16}$$

where E_d and E_a are the surface diffusion and the desorption activation energies, respectively, R is the universal gas constant, and T is the temperature. Both E_d and E_a increase with N. The corrugation ratio $\beta = E_d/E_a$ has been found by Brand et al.[5] to be equal to ≈ 0.3 for a series of n-alkanes on Ru (001) or about twice as large as the value 0.12 – 0.15 often accepted for physisorbed species. They also showed that the pre-exponential factor D_0 was practically independent of N and attributed these findings to peculiarities of polyatomic molecules binding to the surface. With $D = b\tau_a^{-\beta}$ from Eq. (16) and $b = D_0\tau_0^{-\beta} \approx$ const, the product Dn_∞ can be written as the following function of the residence time

$$Dn_\infty \equiv F(\tau_a) = \frac{b\,\tau_a^{-\beta} J_{vap}}{J_{vap}/n_0 + \tau_a^{-1}} \tag{17}$$

This quantity attains the maximum value at

$$\tau_a = \frac{n_0}{J_{vap}} \frac{1-\beta}{\beta} \tag{18}$$

The maximum of $F(\tau_a)$ should be attributed to molecular species playing the major role in the deposition process and consisting of a certain number N_m of carbon atoms. The experimental results discussed in Section 4.2 can be best explained assuming $N_m = 10$. Smaller molecules do not produce sufficient surface coverage whereas larger ones are too slow and lose in competition with their lighter counterparts which are more mobile. Inserting τ_a from Eq.(18) into (15) yields

$$n_\infty = (1-\beta) n_0 \approx 0.7 n_0 \tag{19}$$

Assuming that the deposit is composed of polymerized molecules with n_∞ determined by Eq.(19) we can relate the measured deposition rates with diffusion coefficients as follows

$$\frac{dN_{dep}}{dt} \approx 1.4\pi n_0 p \frac{D}{1+1/q} \qquad \text{for } D = \text{const} \tag{20a}$$

$$\frac{dN_{dep}}{dt} \approx 1.4\pi n_0 p \frac{D_1}{1+D_1/qD_2} \qquad \text{for } D_1 \neq D_2 \tag{20b}$$

where $q \approx 10$ and p is determined by formulas (13). The advantage of Eq. (20b) compared to Eq. (14) is that the latter does not contain the unknown quantity n_∞ and hence can be used to determine diffusion coefficients from the measured deposition rate.

The choice of whether the surface diffusion coefficient might be considered constant or not, depends on the ratio of the deposition rates for pillars and rings

$$m \equiv \frac{dN_{dep,pillar}}{dt} \Big/ \frac{dN_{dep,ring}}{dt} = \frac{dV_{pillar}}{dt} \Big/ \frac{dV_{ring}}{dt} \tag{21}$$

In the case of similar diffusion conditions on the substrate and deposit, we have

$$m = \frac{L^+_{pillar}}{L^+_{ring}} = \frac{p_{pillar}}{p_{ring}} \approx 1/3 \qquad \text{for } D = \text{const} \tag{22}$$

Physically, the values of $m < 1$ for a homogeneous surface are expected for the following reasons. Molecules impinged on the surface at distances smaller than about $2\lambda_1$ from the BIR of radius R and performing random motion can either desorb prior to crossing the border at $r = R$ or penetrate inside the BIR and get attached to the polymer network. The probability of the first event increases with decreasing R, resulting in $L^+_{pillar} < L^+_{ring}$ and $m < 1$. Contrary to these expectations, the volumetric growth rates of pillars in our experiments were always larger than those of ring-like deposits. The largest value of $m \approx 12$ was obtained from comparison of the measured deposition rates for rings and pillars on the freshly cleaved HOPG surface. These results obviously disagree with the assumption of constant D.

According to Eqs. (8),(10), (20b), both n_R and L^- increase with decreasing ratio D_2/D_1, while the deposition rate drops off. As shown below, the values of $q \approx 10$ and $D_1/D_2 \sim 10^2$-10^3 match our experimental data for ring-like deposits indicating at least tenfold increase of n_R and L^- compared to the case D = const. In the limiting case $D_2 \rightarrow 0$, the density gradient on the unexposed surface vanishes and molecules do not penetrate into the BIR from the surrounding area, hence the rate of their dissociation goes to zero. A similar effect can be attained by an imaginary reflecting barrier at the sharp edge of the BIR with flat-top current density distribution. Hence, the border between two areas with different diffusion conditions can be considered as a virtual additional barrier for diffusion. This effect is schematically illustrated in Figure1. Ring-like and pillar-like features grow predominantly on thin and bulk substrates, respectively.

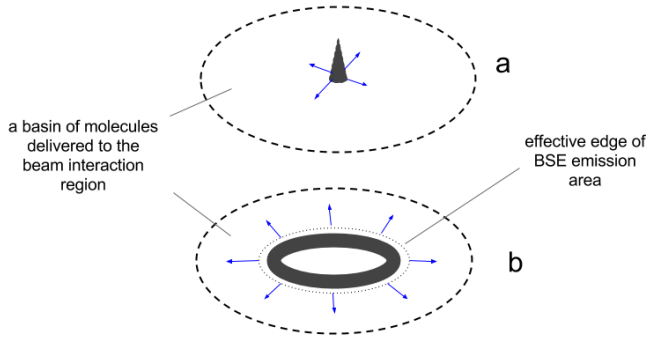

Fig. 1. Schemes of EBID of carbon on thin (a) and bulk (b) substrates. Arrows illustrate repulsion of molecules from the virtual barrier separating regions with different diffusion conditions ($D=D_1$ on the bare substrate and $D=D_2<D_1$ on the deposit). The fraction of molecules returning from the edge of the BIR to the surrounding area increases with D_1/D_2 ratio.

3. Experimental

EBID experiments were performed using a Carl Zeiss 1540-XB dual electron-ion beam system equipped with secondary ion mass spectrometer. The chamber was evacuated by a turbomolecular pump down to a pressure of $1\text{x}10^{-6}$ to $3\text{x}10^{-7}$ Torr. Residual gas analysis (RGA) was carried out for molecular masses within a range of 5 to 300 amu (atomic mass units). Water and nitrogen were the main components of the residual atmosphere; the total fraction of organics was estimated to be 10 to 20%.

Carbon ring-like and pillar-like features were grown on bulk and thin substrates irradiated by a focused electron beam of ~1 nm radius at a beam energy of 20 keV and beam currents I_{PE} ranging from ≈10 to ≈300 pA. Silicon (100) wafers, GaAs (100) crystals grown by molecular beam epitaxy (MBE), and freshly cleaved pieces of highly oriented pyrolytic graphite (HOPG) were used as bulk substrates. The choice of substrates was dictated by the high degree of their smoothness. To prepare smooth thin substrates, carbon rods were arc evaporated onto cleaved KCl crystals to produce coatings of 40 to 200 nm thickness. Carbon films were then detached from KCl in distilled water, picked up on copper grids and mounted on the SEM stage. Using thin carbon films as substrates allowed a reduction of the BSE emission practically to zero and led to a manifold decrease of the effective BIR diameter.

In another set of experiments aimed at determining the effect of surface roughening on diffusivities of adsorbed n-alkanes, gold was thermally evaporated onto initially smooth substrates to produce a film of 60 to 100 nm thickness. The surfaces of discontinuous gold films were extremely corrugated and exhibited irregular pits and cracks of more than 10 nm depth. Intuitively, it was expected that diffusing molecules would be much more mobile on smooth

surfaces than on corrugated ones. Contrary to these expectations, no remarkable reduction of the diffusive flux with increasing rms surface roughness has been noticed.

At the end of the deposition process, the specimens were extracted from the SEM chamber and fixed on the stage of an atomic force microscope (AFM) operated at atmospheric pressure. The vertical and lateral dimensions of the deposited features were measured either on SEM images of tilted specimens or by analyzing surface profiles obtained with an AFM.

4. Results and discussion

4.1. Deposit shapes

The shapes and dimensions of carbon deposits varied depending on the substrate and the beam current. The typical pillar-like and ring-like shapes are illustrated in Figures 2 and 3. Ring-like features were observed on bulk substrates while pillars grew on thin self-supporting films. The only exception was the surface of a freshly cleaved HOPG on which pillars grew during several seconds at the beam current of 300 pA and then disappeared [14].

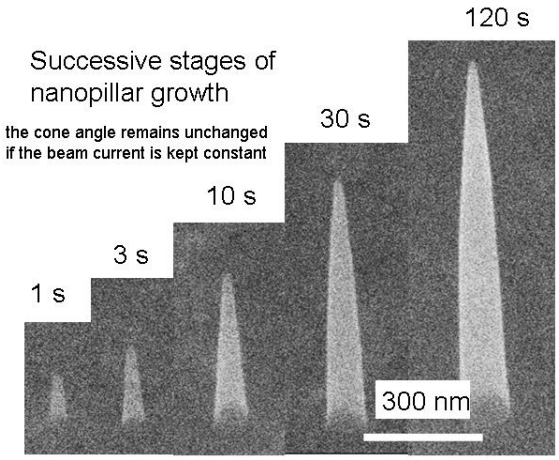

Fig. 2. Tilted SEM images illustrating evolution of carbon nanopillars grown on a thin self-supporting amorphous carbon film at a beam current of 10 pA.

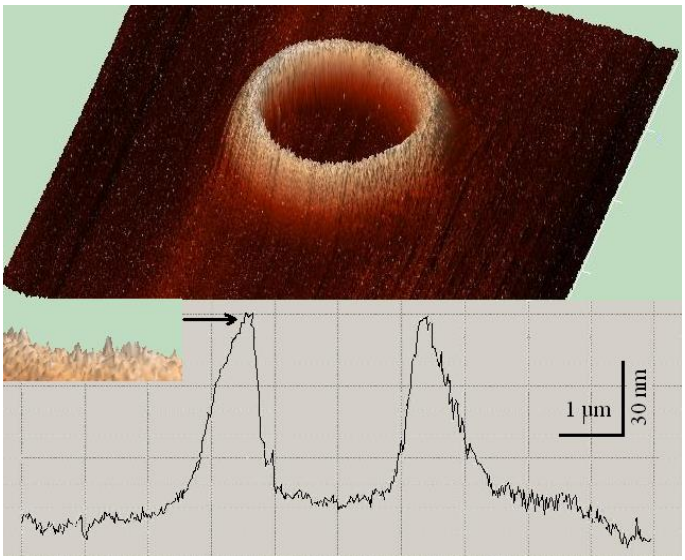

Fig. 3. AFM image and cross sectional profile of a carbon deposit on GaAs (100). An enlarged cross sectional image of the ring is shown in the inset. Note different scales along horizontal and vertical axis. The largest protrusions on the ring surface have a height of about 2 nm

The nearly ideal conical shapes of pillars shown in Figure 2 are believed to reproduce spatial distribution of scattered primary electrons (PE) in solid carbon. At the start of the deposition process, dissociation of molecules occurs mainly due to secondary electron (SE) emission from the substrate leading to pillar broadening at the base. Small aspect ratio pillars were observed on graphite surface during several first seconds of the growth. Pillars of rounded shapes resembling rotational ellipsoids grew on the bottom side of the self-supporting carbon film where the beam spot was considerably larger than on the top surface due to the scattering of PE by passing through the film. To make the problem of the electron-adsorbate interaction on the lateral surfaces of pillars analytically tractable we approximated their shapes by cones in all cases. The angle between the vertical plane and the tangent to the pillar sidewall drawn through the lowest point was considered as analogous to the cone half-angle $\alpha/2$.

4.2. Molecular species participating in the deposition process

RGA spectrum shown in Figure 4 has a saw-like profile indicating presence of n-alkanes with molecular masses M differing by 14 amu (atomic mass units). The peak heights fall with increasing number N of carbon atoms in a chain for $N \leq 10$ and then approach saturation. Similar behavior was observed by Hollenshead and Klebanoff [15] for hydrocarbons present in a slightly contaminated ultra-high vacuum chamber.

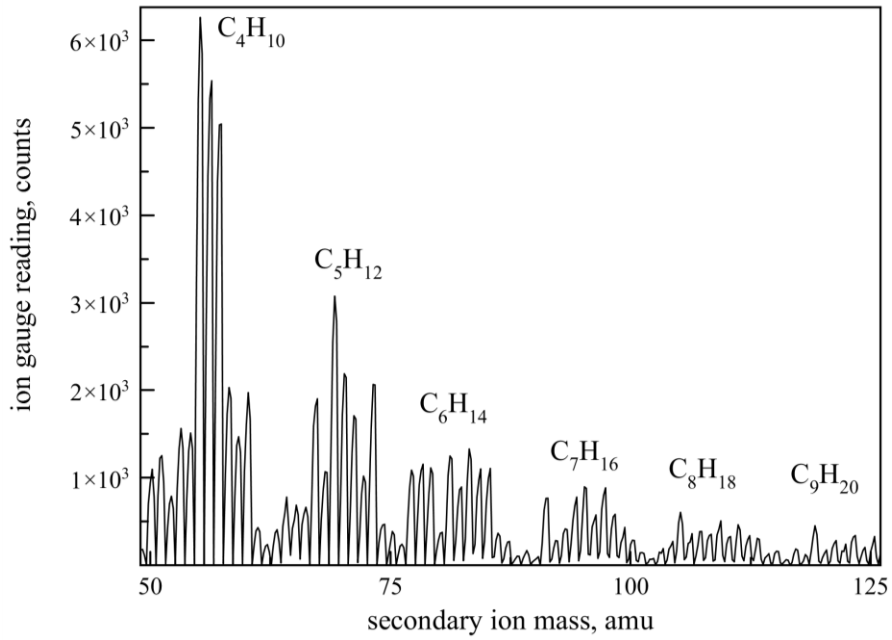

Fig.4. Ion currents plotted versus ion mass at a section of the residual gas analysis (RGA) scan. Peaks separated by 14 amu indicate presence of n-alkanes in the specimen chamber.

Comparing the integrated ion currents related to each n-alkane with currents produced by ionized water and nitrogen molecules we estimated the partial pressure for molecular species of $M \approx 130$ amu to be equal to about $3\text{x}10^{-9}$ Torr. According to the classical kinetic theory of gases this value corresponds to the flux $J_{vap} \approx 5\text{x}10^{11}$ molecules /cm^2 s at room temperature. Setting $n_0 = 2\text{x}10^{14}$ cm^{-2} and $\beta = 0.3$ in Eq. (18), we get the following estimate for the residence time of molecules playing the key role in the deposition process

$$\tau_a = \frac{0.43 n_0}{J_{vap}} \approx 9x10^2\, s \qquad (23)$$

The theoretical estimates of τ_a for various N can be obtained from the Arrhenius expression $\tau_a = \tau_0 \exp(E_a/RT)$ using desorption activation energies E_a from the literature. Experiments performed with a number of n-alkanes on various surfaces in well defined conditions gave evidence that addition of one methylene unit to a molecule led to 7±1 kJ/mol increase in desorption energy E_a [5, 6, 16]. Using molecular dynamic simulation to mimic desorption of n-alkanes from Au (111), Fitchhorn and Miron [17] suggested a slightly steeper increase of E_a with N. They found $E_a \approx 100$ kJ/mol for N =10, very close to the value obtained experimentally for n-decane desorption from the basal plane of graphite in Ref. [16].

There is no common agreement concerning the value of the prefactor τ_0.(the inverse attempt frequency) in the Arrhenius expression, According to [17], prefactors τ_0 for large molecules might be significantly smaller than the typical value 10^{-13} s and probably range from $\sim 10^{-15}$ to $\sim 10^{-16}$ s for n-alkanes with N = 6 to 12 carbon atoms. The values of $\tau_0 \sim 10^{-15}$s were suggested for smaller n- alkanes (N = 3 to 6) on Ru (100) [5].

In Figure 5, plots of τ_a versus N are drawn using activation energies for n-alkanes desorption from graphite [16] and Au (111) [17] with τ_0 ranging from 10^{-14} to 10^{-15} s. The intersection of these plots with a horizontal line $\tau_a = 9x10^2$s occurs at $N \approx 10$ pointing to n-decane as a species mostly responsible for contamination layer built up in our case.

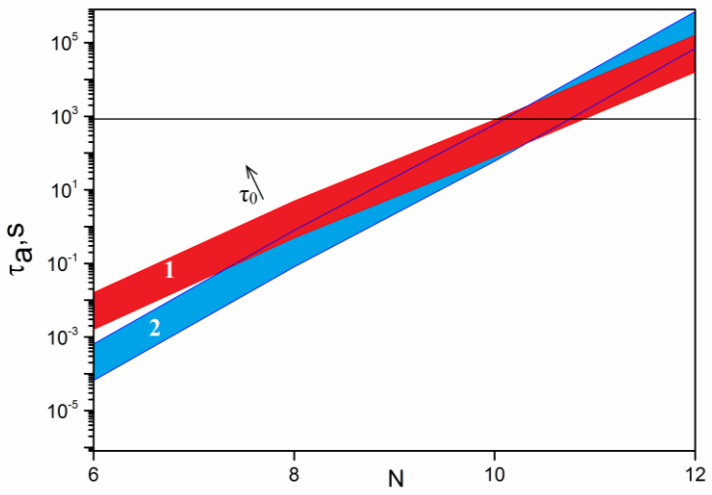

Fig.5. Residence times of n-alkane adsorbate molecules plotted versus the chain length using activation energies E_a for desorption from HOPG (1) and Au(111) (2). The values of E_a are taken from Refs. [16, 17]. The colored stripes correspond to the range of inverse attempt frequencies τ_0 from $1x10^{-14}$ to $1x10^{-15}$ s. The intersection of the plots with the horizontal line drawn through the point $\tau_a = 9x10^2$s (see formula (23)) occurs at $N \approx 10$. This value is assumed equal to the number of C atoms in hydrocarbon molecules mostly participating in the deposition process.

Using a quite different approach and assuming $\tau_0 = 10^{-13}$ s, Hollenshead and Klebanoff [15] suggested n-nonane (N = 9) as a species playing the key role in contamination of extreme ultraviolet optics with ruthenium capping layer. The small discrepancy between their conclusions with ours might well be caused by a different choice of the value of τ_0. Decreasing τ_0 would bring larger molecules to the fore. Interestingly, despite a large variety of residual hydrocarbons with

complex binding geometries on various substrates, only one or two species might be mostly responsible for the contamination phenomenon, the latter being fairly independent of the substrate material.

4.3. Parameters characterizing SE–adsorbate interactions. Preliminary rough estimates of D_2.

There are considerable grounds to believe that low-energy secondary electrons (SE) dominate in the EBID process [18,19]. These are generated at various distances from the beam incidence point by inelastically scattered primary electrons (PE) or by backscattered electrons (BSE) and are commonly denoted SE1 and SE2, respectively.

The outer radii of carbon rings grown on various substrates studied in this work correlate with the BSE ranges predicted by the theories of electron scattering in solid targets [20, 21]. Eq.(C1),(C2) relate the SE2 current ejected from a ring of inner and outer radii r_1 and r_2 , respectively, with the mean square deviation a of the BSE lateral distribution.

We will consider Si wafer irradiated at E_0 =20 keV and I_{PE} =300 pA as an example. Setting η= 0.16, δ = 0.4, $a \approx 1$ μm, $r_1 \approx 2.5$ μm , $r_2 \approx 4$ μm, one obtains the following estimates for the total SE current, the mean current density and the emission rate from the ring area S_{ring}:

$I_{SE} = 4.5\text{x}10^{-13}$ A, $\langle J_{SE} \rangle = I_{SE}/S_{ring} = 3.2\text{x}10^{-6}$ A/cm^2, $dN_{SE}/dt \approx 6\ \text{x}10^6$ electrons/s.

The ratio of the latter quantity to the calculated deposition rate $dN_{dep}/dt = 6.5\text{x}10^5$ molecules/s gives the average number of SE required for dissociation of one molecule (≈ 10 in our case).The inverse quantity γ is introduced in Appendix C to characterize the efficiency of the beam-precursor interactions.

Using formulas (3), (4), the deposition rate can be written as follows

$$\frac{dN_{dep}}{dt} \approx \frac{< n >}{< \tau_j >} S_{ring} = \gamma \frac{dN_{SE}}{dt} \qquad (24)$$

The density of diffusing molecules traversing the ring area drops off from n_R at $r = r_1 = R$ approximately to zero at $r = r_2$. With $\langle n \rangle \approx n_R/2$, $dN_{SE}/dt = I_{SE}/e$, $\langle \tau_j \rangle = I_{SE}/\sigma S_{ring}$, the approximate expression for the dissociation cross section σ takes the form

$$\sigma \approx \frac{2\gamma}{n_R} \qquad (25)$$

The maximum interaction efficiency (γ = 1) corresponds to the case of full monolayer surface coverage by precursor molecules with $\sigma_{max} \approx S_{molecule} = 1/n_0$. Typically, $\sigma < S_{molecule}$, and $\gamma << 1$. These inequalities impose restrictions to the possible values of σ and n_R. For example, if γ = 0.1 and $n_0 = 2\text{x}10^{14}$ cm^{-2}, σ should be larger than $1\text{x}10^{-15}$ cm^2 to make n_R physically meaningful for the case of monolayer adsorption. With $n_R < n_\infty = 0.7\ n_0$, $\sigma_{max} \approx 1/n_0$, $\langle J_{SE} \rangle = 3.2\text{x}10^{-6}$ A/cm^2, the windows for σ and $\tau_j \equiv \langle \tau_j \rangle$ are

$$1.4\text{x}10^{-15}\ \text{cm}^2 < \sigma < 5\text{x}10^{-15}\ \text{cm}^2 \qquad (26)$$
$$14\text{s} < \tau_j < 50\text{s}$$

Inserting the mean values $\tau_j \approx 30$s, $\lambda \approx (r_2\text{-}r_1)/2 \approx 0.7$ μm into the definition of the diffusion length, yields the surface diffusion coefficient of adsorbed molecules on the ring-like carbonaceous deposit formed on Si (001) at $T \approx 300$ K as follows

$$D_{2,ring} = \left(\frac{\lambda^2}{\tau_j} \right)_{ring} \approx 2x10^{-10} cm^2 s^{-1} \qquad (27)$$

On thin substrates with negligible BSE emission, molecules are dissociated by SE1 ejected either from a substrate area close to the beam incidence point or from the growing pillar. The laws of electron beam scattering in solid targets are widely discussed [20, 21]. We used Eqs.(6, 7) from Ref. [22] to estimate the PE current density on the horizontal plane at the depth of h ≈ 1μm in amorphous carbon and obtained $J_{PE} \approx 3x10^{-3}$ A cm^{-2} for I_{PE} = 300 pA. To estimate the SE1 current density, J_{SE}, two additional factors should be accounted for. First, the current density on the cone sidewall is about 2/α times smaller than on the horizontal plane, α being the cone angle. Second, emission of each PE at a grazing angle is accompanied by emission of a certain number Y of SE1. For a crude estimate we took the value of Y ≈ 5 obtained by Monte Carlo simulation of electron scattering in a growing pillar [23]. Setting α = 0.1 rad and taking the mean value $<\sigma> \approx 3x10^{-15}$ cm^2 from window (26) yields

$$J_{SE} = (2/\alpha) Y J_{PE} \approx 7x10^{-4} \text{ A cm}^{-2}$$

$$\tau_j = e/<\sigma> J_{SE} \approx 0.08 \text{ s}$$

$$D_{2,pillar} = \left(\frac{\lambda^2}{\tau_j} \right)_{pillar} \approx 4x10^{-8} cm^2 s^{-1} \qquad (28)$$

Here $\lambda = r_{base}/\alpha \approx 600$ nm is the diffusion length of molecules on the lowest section of a conical pillar with the base radius r_{base} = 60 nm (according to Eq.(B4)) and $D_{2,pillar}$ is the surface diffusion coefficient on the sidewall of a carbon pillar grown on the top surface of amorphous carbon film at $T \approx 300$ K.

The difference of two orders of magnitude between diffusion coefficients on the ring-like and pillar-like deposits greatly exceeds any imaginable summarized effect caused by approximations involved in the calculation. We suggest that the increase of the diffusion coefficient on the pillar sidewall compared to that on the planar deposit results from decrease of surface roughness. AFM profiles of carbon rings prove presence of numerous nanometer high protrusions as illustrated by the inset in Figure 3. We could not obtain similar profiles of carbon pillars with lateral dimensions comparable to the curvature radius of the AFM probe, however, no irregularities were detected on SEM images of pillars at ~1nm spatial resolution. We expect that pits and protrusions of molecular dimensions which appear on any irradiated surface as a result of the stochastic nature of the deposition process are then smoothed away on the pillar sidewalls due to higher current densities and hence higher probabilities of molecules to be pinned at points closest to the beam axis.

4.4. Relations between deposition rates and diffusion coefficients D_1 and D_2

As suggested in the previous section, there are different diffusion conditions on the surfaces of carbonaceous rings and pillars. For this case, Eq.(20b) should be replaced by a pair of equations in the form

$$\left(\frac{dN_{dep}}{dt} \right)_{ring} = 1.4\pi p_{ring} n_0 \frac{D_1}{1 + D_1 / qD_{2,ring}} \qquad (32)$$

$$\left(\frac{dN_{dep}}{dt}\right)_{pillar} = 1.4\pi p_{pillar} n_0 \frac{D_1}{1 + 2D_1/\alpha q D_{2,pillar}} \quad (33)$$

where $D_{2,ring}$ and $D_{2,pillar}$ are diffusion coefficients on rings and pillars, respectively. The term $2/\alpha$ in the denominator of the last equation is introduced to account for the increase of the diffusion coefficient on the flanks of a cone compared to that on the plane surface, in accordance with Eq. (B4).

Dividing Eq.(33) by Eq.(32) yields the surface diffusion coefficient on the substrate

$$D_1 \approx \frac{(3m-1)qD_{2,ring}}{1 - 6m/\chi\alpha} \quad (34)$$

with

$$\chi \equiv \frac{D_{2,pillar}}{D_{2,ring}} \quad (35)$$

Here m is the experimental ratio of the volumetric growth rates of the pillar-like and ring-like deposits and $q \approx 10$ is the numerical factor determined by Eq.(A6).We took $w = p_{ring}/p_{pillar} \approx 3$ from (22). The measured deposition rates on various substrates are listed in Table 1.

Deposition rates (molecules/s) were determined from the measured volumetric growth rates assuming a molecular volume $\Omega = 0.125$ nm^3. Since no remarkable dependence of the volumetric growth rates of ring-like deposits on the substrate material has been found, it is possible to use the mean value $(dN_{dep}/dt)_{ring} = (6.5 \pm 1.5)\text{x}10^5$ molecules/s for all substrates. The ratio m increased from about 1.6 on the top surface of a carbon film to about 12 on the HOPG surface. For $D_1 >> qD_{2,ring}$, Eq. (32) reduces to

$$\left(\frac{dN_{dep}}{dt}\right)_{ring} = 1.4\pi p_{ring} n_0 q D_{2,ring} \quad (36)$$

Setting $(dN_{dep}/dt)_{ring} = 6.5\text{x}10^5 \text{s}^{-1}$, $p_{ring} = 0.6$, $n_0 = 2\text{x}10^{14}$ cm^{-2}, $q = 10$ yields

$$D_{2,ring} \approx 1.3x10^{-10} cm^2 s^{-1} \quad (37)$$

in agreement with the estimate of $D_{2,ring}$ by formula (27). Good coincidence of two values obtained from two sets of diverse parameters gives additional proof to the validity of the approximations used in the calculations. The most accurate value of $\alpha \approx 0.1$ rad was determined for the set of pillars grown on the top side of the thin carbon film with $m \approx 1.6$. Since the denominator in Eq. (34) is always positive, we obtain $\chi \geq \chi_{min} \approx 1\text{x}10^2$ for this case.

The admissible ranges of D_1 and $D_{2,pillar}$ are restricted from below by

$$D_{1,min} = (3m-1)qD_{2,ring} \approx 1.2x(3m-1)x10^{-9} cm^2 s^{-1} \quad (38)$$

$$(D_{2,pillar})_{min} = \chi_{min} D_{2,ring} \approx 1x10^{-8} cm^2 s^{-1} \quad (39)$$

Comparison of formulas (29), (39) again shows a fair agreement of D_2 values predicted by the two different approaches.

Table 1 Parameters characterizing EBID of carbon at E_0=20 keV, I_{PE}=300 pA on the substrates used in this work.

Substrate material, orientation, and minimum measured roughness {R_q (nm)}	Deposit shape	Deposition rate, dN_{deo}/dt (molecules /s)	Maxim. vertical growth rate, $(dh/dt)_{max}$ (nm/s)	Diffusion coefficients at room temperature, D(cm^2/s)			Comments
				on the deposit $D = D_2$	on the substrate, $D = D_1$		(A) - calc. from Eq.(20a) for $D = const$ (B) – $D_{1,min}$ calc. from Eq. (38) for $D_1 >> D_2$
					(A)	(B)	
Si (100) {0.39}	ring	6.5×10^5	4.0×10^{-3}	1×10^{-10}	1.3×10^{-9}		comparable D_1 values ($D_1 > 4\times10^{-8}$ cm^{2}s^{-1}) are expected for substrates (Si, GaAs, HOPG) with similar roughness
GaAs (100) {0.36}	ring	8.0×10^5	2.0×10^{-2}	1×10^{-10}	1.1×10^{-9}		
HOPG (0001) {0.33} a) t < 10 s	sharp conical pillar	6.0×10^6	3.5×10^2	3×10^{-8}	1×10^{-9}	4×10^{-8}	Deposition slows down and turns into etching
b) t≥3 min	ring	5.0×10^5	3.0×10^{-3}	1×10^{-10}	1×10^{-9}	4×10^{-8}	Typically two rings with radii differing by ~20%
HOPG +60nm Au {7,5}	ring	3.0×10^5	2.7×10^{-3}	1×10^{-10}	6×10^{-10}	2×10^{-9}	Numerous pits and cracks
Self-supporting amorphous carbon film a)top surface	conical pillar with a broad base	1.0×10^6	3.0×10^2	3×10^{-8}		7×10^{-9}	No direct measurements of surface roughness were performed but 10 to 100 nm inhomogeneities were observed on the upper side of the film and were absent on the opposite side
b)bottom surface	ellipsoidal pillar	3.0×10^6	7.0×10^1	3×10^{-8}		2×10^{-8}	

Notes to Table1

1) R_q is the minimum rms surface roughness measured with an AFM over the area ~ 1μm^2
2) The upper limits of D_1 on various surfaces could not be determined but were assumed to be several times higher than the values of $D_{1,min}$ measured on the same substrates with pillar-like deposits.

3) The difference between calculated values of D_2 on pillars and rings is most likely due to the smaller surface roughness of the former. The value of $D_{2,pillar}$ was obtained from (35) assuming $\chi \approx 2x10^2$ and $D_{2,pillar} \approx 1.3x10^{-10}$ cm^2s^{-1}.
4) The transformation of the pillar shape from a cone to a rotational ellipsoid on the bottom side of a carbon film was caused by the broadening of the beam by passing through the film.

Eq. (34) does not allow to determine D_1 without the exact knowledge of χ. In the extreme case where χ approaches χ_{min}, D_1 diverges, and the deposition rate becomes independent of D_1. This behavior can hardly be expected considering the spread of deposition rates determined experimentally on different surfaces with pillars. Besides, decreasing difference between χ and χ_{min} requires a very special combination of deposit shapes to be sustained on various surfaces. The experimental results presented in Table 1 best correspond to the theoretical predictions under assumption that the values of D_1 and $D_{2,\ pillar}$ are comparable. For example, setting $\chi = 2x10^2$ and $6m/\alpha \approx$ const $= 1x10^2$ would give D_1 ranging from $\sim 1x10^{-8}$ cm^2 s^{-1} on the top side of carbon film to $\sim 1x10^{-7}$ cm^2 s^{-1} on the HOPG surface, whereas the value of $D_{2,\ pillar}$ lies between.

Comparing the values of D_1 and $D_{2,\ pillar}$ one should bear in mind that they relate to diffusion over areas differing by about four orders of magnitude. The molecules delivered to the BIR from surrounding areas encounter dozens of steps separating flat terraces as shown in Figure 6a. Traversing steps inevitably leads to a diffusion slowdown. The difference between intrinsic (over flat terraces) and mass-transfer (over large distances on inhomogeneous surfaces) diffusion coefficients is common for various systems [26]. Hence, we expect that the surface diffusion coefficient of n-decane molecules on atomically flat terraces on HOPG may be substantially higher than the value of
$1x10^{-7}$ cm^2s^{-1} given above.

4.5. The roles of substrate material and surface roughness

We have found no considerable dependence of the volumetric growth rates of ring-like deposits on the substrate material. Such behavior might be expected from Eq. (32) for substrates with the surface diffusion coefficient greatly exceeding that on the contamination layer. Besides, large organic molecules should be much less sensitive to elemental composition and arrangement of surface atoms than molecules consisting of only a few atoms [17].

The effect of surface roughness is more complicated as shown by Figures 5-7. On the one hand, manifold increase of rms (root mean squared) roughness of initially smooth surfaces after coating by a discontinuos gold layer had but a little effect on the growth rate of carbon rings.

On the other hand, ~0.1 ML coverage of atomically flat terraces on an HOPG surface by a contamination film caused a remarkable reduction of the growth rate of carbon pillars leading to complete cessation of the growth in some cases. The likely explanation is that clusters consisting of several polymerized molecules act as traps hampering surface diffusion. The estimated density of immobile clusters at 0.1 ML coverage equals to $\sim 10^{12}$ cm^{-2}, less than the density of $\sim 10^{13}$ cm^{-2} of diffusing molecules and much higher than the measured density of $\sim 10^{10}$ cm^{-2} of large-scale inhomogeneities (pits and cracks of several dozen nanometers deep) on gold coatings.

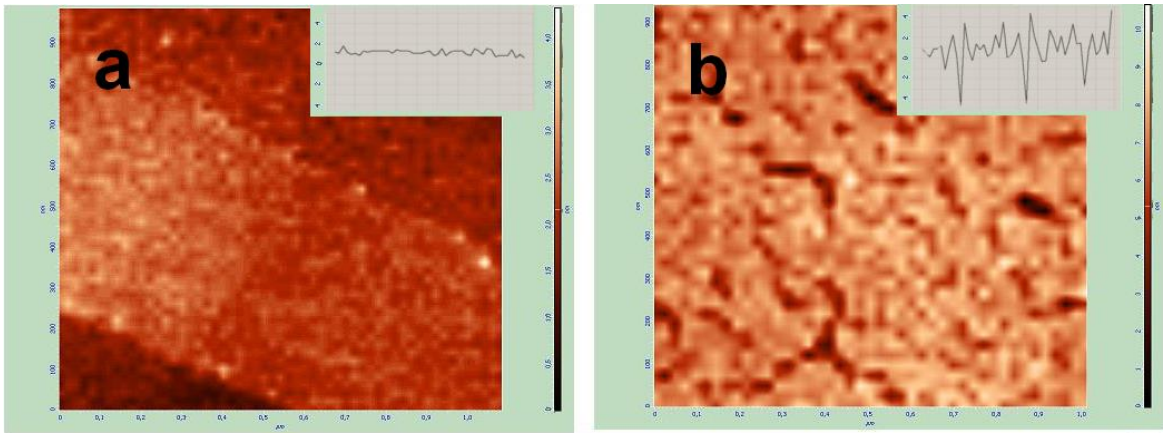

Fig. 6. AFM images and cross sectional profiles of the surfaces of HOPG (highly oriented pyrographite) (a), and 60 nm thick gold layer on HOPG (b). Stripes of different grey level are atomically smooth terraces on the freshly cleaved HOPG. High-frequency contrast variations are probably due to uncontrolled physisorbed species present on the samples in the AFM operated at atmospheric pressure. Cross sectional profiles are shown in the insets. Deviations from the zero level in the insets are in nanometers. Carbon deposition rates on both substrates were comparable contrary to intuitive expectations of much higher deposition rate on the substrate (a) compared to that on (b) for the case of diffusive molecular transport.

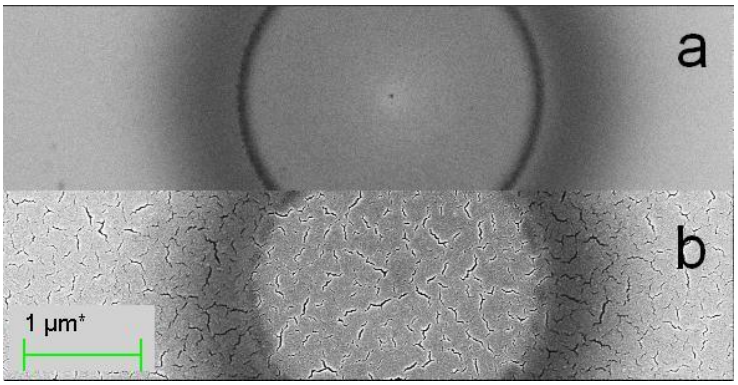

Fig. 7. SEM images of carbon rings on uncoated (a) and covered by 100 nm Au (b) GaAs (100) crystals. Coincidence of positions and widths of the rings on images (a) and (b) proves that delivery rates of molecules to the BIR were approximately equal in both cases despite a manifold increase of the substrate roughness on (b). Wormlike streaks on (b) are irregular trenches of several tens nm depth.

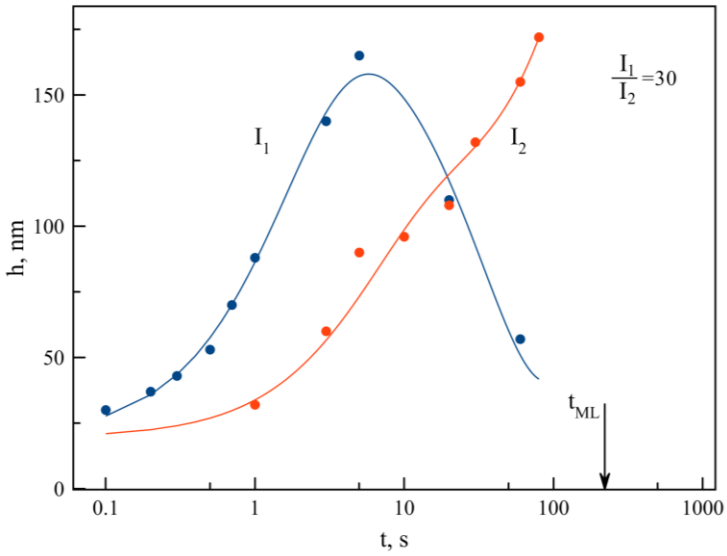

Fig.8. Carbon nanopillar heights on HOPG plotted versus deposition time at two different beam currents. Transition from growth to evaporation at larger beam current occurs due to a dramatic decrease of the molecular diffusion flux towards the beam incidence point on the progressively contaminated substrate. Expected time of full surface coverage by the contamination layer is indicated by the arrow.

We assume that the effect of traps on the diffusion rate is manifested when the delay time of a molecule on a trap is much longer than the time required to overcome the distance between two adjacent traps by random walk. It takes ~ 10^{-4} s and ~10^{-2} s for a molecule on a surface with a diffusion coefficient D = 4x10^{-8} cm^{2}s^{-1} to pass the distances 10 nm and 100 nm, respectively. Hence, one may expect that the molecules spending a medium time 10^{-3}s in a bound state at one of defects with density of 10^{-10} cm^2 would be delivered to the BIR from about the same area as on the perfect surface leaving the deposition rate unchanged. On the contrary, increasing the density of defects to ~ 10^{12} cm^{-2} might be accompanied by two orders of magnitude decrease of the deposition rate. An expression for the delay of molecules at defects can be written in terms of the binding energy E_b as $t_b = \nu_0^{-1} \exp(E_b/kT)$, where t_b is the delay time and ν_0 is the attempt frequency. Setting t_b =10^{-3}s, ν_0 = 10^{14} s^{-1}, T =300 K we get $E_b \approx 0.6$ eV, about twice as large as the activation energy for diffusion of n-decane molecules over a perfect surface. Doubling of the activation energy seems quite reasonable when a molecule is aligned with the carbon chain backbone parallel to the linear obstacle to maximize the efficiency of van der Waals interactions.

5. Conclusions

The growth kinetics of carbon micro- and nanostructures produced by EBID on bulk and thin substrates has been studied. Experiments were performed under conditions where surface diffusion was the dominant mechanism for transferring hydrocarbon molecules to the BIR. We modified the theory [3] of specimen contamination to explain different attachment rates of molecules to ring-like and pillar-like deposits. The correlation between deposition and diffusion rates predicted by the modified theory was used to estimate the surface diffusion coefficients D_1 and D_2 outside and inside of the BIR, respectively. Among various residual hydrocarbons, n-decane was suggested to be the key participant in the deposition process.

No remarkable dependence of deposition rates on the surface material has been found. This behavior might be caused by peculiarities of polyatomic molecules binding to a host substrate of another material where only a fraction of adsorbate atoms reside in deepest potential minima while other atoms do not. As a result, a molecule travels in a potential field averaged over a large number of surface sites. Using predictions [17] based on molecular dynamic simulations, “the discreetness of the substrate lattice becomes less significant as the size of a molecule increases”. Another explanation suggested in the present work takes into account a dependence of the deposition rate on both D_1 and D_2. For large D_1/D_2 ratios deposition rate depends mostly on the diffusion conditions on the deposit rather than on the unexposed surface. The boundary between two areas with different diffusion coefficients might be considered as a semi-transparent wall with the reflection coefficient being a function of D_1/D_2.

We consider the density of surface defects of molecular dimensions as the crucial parameter determining mobility of n-alkane molecules. In our experiments performed with freshly cleaved graphite crystals the growth rate of carbon nanopillars fell dramatically at ~0.1 ML coverage of atomically flat terraces by hydrocarbon contaminants. Under these conditions the contamination layer consisted of discrete clusters of polymerized molecules with a density of ~10^{12}-10^{13} cm^{-2}. These act as effective traps hampering surface diffusion. In contrast, coating of initially smooth substrates by discontinuous gold films with ~ 10^{-10} cm^{-2} pits of several dozen nanometers deep had no remarkable effect on the deposition rate suggesting the densities of surface defects rather than their vertical dimensions to be of major importance. Molecules seem to overcome large and comparatively rare obstacles rather easily while being delayed by numerous protrusions of atomic

height. Crude estimate of molecular binding energy at linear defects gives a value about twice as large as the activation energy of surface diffusion.

A strong dependence of the deposition rates on surface roughness might be the cause of a large spread of diffusion parameters estimated from EBID experiments performed under poorly controlled conditions [10].

Acknowledgements

The authors would like to acknowledge T.V. Sharov and Yu.K. Dolgikh for providing HOPG and GaAs samples, and A.D. Manukhova for participating in experiments with HOPG.

Appendix A. Solution of the steady-state mass-conservation equation

The analytical solution of Eq. (5) was obtained by Müller [3] for the simplest case of uniformly irradiated circular area of radius R under boundary conditions

$$n(r \to \infty) = n_\infty ; n(r = R) = n_R ; \frac{dn_1}{dr}(r = R) = \frac{dn_2}{dr}(r = R); \frac{dn_2}{dr}(r = 0) = 0$$

where n_1 and n_2 are the densities of adsorbate molecules for $r \geq R$ and $r \leq R$, correspondingly, r is the radial distance from the beam incidence point.

In a more convenient form and with different notations than in Ref. [3], the final result can be represented as

$$n_1 = n_\infty \left[1 - \frac{K_0(r/\lambda_1)}{K_0(R/\lambda_1)} \right] + n_R \frac{K_0(r/\lambda_1)}{K_0(R/\lambda_1)} \quad \text{(A1)}$$

$$n_2 = n_\infty \left(\frac{\lambda_2}{\lambda_1} \right)^2 \left[1 - \frac{I_0(r/\lambda_2)}{I_0(R/\lambda_2)} \right] + n_R \frac{I_0(r/\lambda_2)}{I_0(R/\lambda_2)} \quad \text{(A2)}$$

where $\lambda_1 = \left(D\tau_{1,eff} \right)^{1/2}$, $\lambda_2 = \left(D\tau_{2,eff} \right)^{1/2}$ (A3)

$$\tau_{1,eff} = \left(\tau_a^{-1} + \frac{n_0}{J_{vap}} \right)^{-1}, \quad \tau_{2,eff} = \left(\tau_a^{-1} + \frac{n_0}{J_{vap}} + \tau_j^{-1} \right)^{-1} \quad \text{(A4)}$$

Here and below $K_0(x)$, $K_1(x)$, $I_0(x)$, $I_1(x)$ are the modified Bessel functions.

The density n_R determined from the boundary condition at the edge of the irradiated area can be written as

$$n_R \approx \frac{n_\infty}{1+q} \qquad \text{for } D\text{=const} \quad \text{(A5)}$$

with a numerical factor q given by

$$q \equiv \frac{\lambda_1}{\lambda_2} \frac{I_1(R/\lambda_2)}{I_0(R/\lambda_2)} \frac{K_0(R/\lambda_1)}{K_1(R/\lambda_1)} \quad \text{(A6)}$$

In the more general case where diffusion coefficients D_1 and D_2 outside and inside of the irradiated area, respectively, are different, the boundary condition takes the form [23]

$$D_1 \frac{dn_1}{dr}(r = R) = D_2 \frac{dn_2}{dr}(r = R) \quad \text{(A7)}$$

It can be easily shown that all previous considerations remain valid in this case, but D in (A3) should be replaced by D_1 and D_2, and q in (A5) by qD_2/D_1. Hence, the density at $r = R$ becomes

$$n_R \approx \frac{n_\infty}{1 + qD_2 / D_1} \qquad \text{for } D_1 \neq D_2 \qquad \text{(A8)}$$

The diffusive flow (the number of molecules per unit time) across the circumference at $r = R$ determined by Fick's first law can be written as

$$L = -2\pi R D_1 \frac{dn_1}{dr}(r = R) = 2\pi D_1 (n_\infty - n_R) \frac{R}{\lambda_1} \frac{K_1(R/\lambda_1)}{K_0(R/\lambda_1)} \qquad \text{(A9)}$$

Appendix B. Absorbate diffusion over a conical nanopillar

When surface diffusion dominates in material transport to the BIR, the terms responsible for direct exchange of molecules between the surface and the gas phase in Eq.(5) can be neglected, and the mass conservation equation for the case D = const can be written as

$$D\left(\frac{1}{r}\frac{d}{dr}\left(r\frac{d}{dr}\right)\right)n = \frac{n}{\tau_j} \qquad \text{(B1)}$$

The Laplacian is written here in extended form to better illustrate its relation to the molecular fluxes across circumferences at r and $r + dr$ on a plane.

To apply a similar approach to diffusion on the surface of a conical pillar with angle α at the apex, the increase of the diffusion path by a factor of 2/α should be taken into account. This requires the replacement of r in Eq. (B1) by $l = 2r/\alpha$, where l is the distance measured from the cone apex (see also [23], where the problem of one-dimensional diffusion on a curved surface has been considered). Then, Eq. (B1) becomes

$$\left(\frac{\alpha}{2}\right)^2 D_{cone}\nabla^2 n = \frac{n}{\tau_{j,cone}} \qquad \text{(B2)}$$

Here and below subscripts are added to distinguish parameters measured on a plane surface and on a cone sidewall.

Eq. (B2) takes the usual form

$$D_{plane}\nabla^2 n = \frac{n}{\tau_{j,plane}} \qquad \text{(B3)}$$

with a set of modified parameters given by

$$D_{plane} = D_{cone}\frac{\alpha}{2},$$

$$\lambda_{plane} = \lambda_{cone}\frac{\alpha}{2},$$

$$\tau_{j,plane} = \tau_{i,cone}\frac{\alpha}{2} \qquad \text{(B4)}$$

For a pillar having a base radius r_{base} and terminating in a cap of radius r_{tip} , Eqs. (B3), (B4) are valid within the range $r_{tip} < r < r_{base}$.

Often, the cone angle remains unchanged or changes only slightly with time, as demonstrated in Figure 2. For this case, the dissociation term, n/τ_j, which determines the lateral growth rate of a pillar during a given time step Δt, is independent of the radial distance r from the

cone axis. Setting $n/\tau_j = const \equiv C$ we obtain the common solution of Eq.(B3) in a surprisingly simple (for a complicated diffusion problem) form

$$n = \frac{Cr^2}{4D_{plane}} = \frac{Cr^2}{2D_{cone}\alpha} \qquad \text{(B5)}$$

We have also

$$\lambda_{plane} = r/2 \qquad \text{(B6)}$$

$$\tau_{j,plane} = r^2/4D_{plane} \qquad \text{(B7)}$$

Appendix C. Efficiency of molecule dissociation by secondary electrons.

As has already been pointed out, ring-like deposits are mostly produced by cracking of hydrocarbons by SE2-type secondary electrons generated by BSE. The lateral distribution of BSE at points not too close to the beam incidence point can be described by a Gaussian [21, 25]

$$J_{BSE}(r) = J_0 \exp(-r^2/2a^2)$$

where J is the current density, r is the radial distance, and a is the mean square deviation. Using this relation, one obtains the total currents of BSE and SE2 emitted from the ring with the outer and the inner radii r_1 and r_2, respectively, in the form

$$I_{BSE} \approx \eta I_{PE} \{\exp(-r_1^2/2a^2) - \exp(-r_2^2/2a^2)\} \qquad \text{(C1)}$$

$$I_{SE} = \delta I_{BSE} \qquad \text{(C2)}$$

Here, I_{PE} is the beam current, η and δ are the backscattering and secondary electron yields, respectively. The latter should be calculated taking into account the broad energy spectrum of BSE. The rate of SE emission can be written as follows

$$\frac{dN_{SE}}{dt} = \frac{I_{SE}}{e} = \frac{< J_{SE} >}{e\pi(r_2^2 - r_1^2)} \qquad \text{(C3)}$$

where e is the electron charge, and $<J_{SE}>$ is the mean SE current density inside of the ring area. We define efficiency of molecule dissociation by secondary electrons as the ratio

$$\gamma = \frac{dN_{dep}/dt}{dN_{SE}/dt} \qquad \text{(C4)}$$

where dN_{dep}/dt is the number of cracked molecules per unit time. Values of $\gamma << 1$ should be expected when deposition proceeds in the so called "mass-transport-limited regime"[10] and the deposition rate is determined by the flow of molecules arriving at the BIR rather than by the beam current.

The growth of pillars occurs due to cracking of molecules by SE-1-type secondary electrons generated by PE. In this case, both the rate of SE-1 emission and the dissociation efficiency γ increase with the pillar height because the area of the cone surface grows with time.

References

[1] R.W.Christy, J.Appl.Phys. **31** (1960), 1680-1683
[2[G.S.Zhdanov, V.N.Vertsner, Doklady Akademii Nauk SSSR. **176** (1967), 1040-1043
[3] K.H.Muller ,Optik, **33** (1971), 276-311
[4] I.Urke, S.Moskalev, P.Russell (Eds.), Nanofabrication Using Focused Ion and Electron Beams. Principles and Applications, Oxford University Press, N.Y., 2012
[5] J.Brand, M.Arena, A.Deckert, S.George. J.Chem.Phys. **92** (1990), 5136-5143
[6] S.M.Wetterer, D.J.Lavrich, T.Cummings, S.L.Bernesek, G.Scoles, J.Phys.Chem. **102** (1998), 9266-9275
[7] A.Szkudlarek, M.Gabureac, I.Utke, J.Nanosci. Nanotechnol. **11** (2011), 8074-8078
[8] J.Cullen, C.J.Lobo, M.J.Ford, M.Toth, ACS Appl.Mater.Interfaces. **7** (2015), 21408-21415
[9] M.Toth, C.J.Lobo, V.FRiedli, A.Szkudralek, I.Utke, *Beilstein* J. Nanotechnol. **6** (2015), 1518-1540
[10] I.Utke, P.Hoffmann, J.Mengalis, J.Vac.Technol.B. **20** (2008), 1197-1276
[11] M.Abramowitz, I.A.Stegun (eds.) Handbook of Mathematical Functions, National Bureau of Standarts. Appl.Math.Series-55, Washington D.C.,1964
[12] Amman, J.W.Sleight, D.R.Lombardi, R.E.Weiser, M.R.Deshpand, M.A.Reed, L.J.Guido, J.Vac.Sci.Technol.B. **14** (1996), 54-62
[13] W.Ding, D.A.Dikin, X.Chen, J.Appl.Phys. 98 (2005), 014905
[14] G.S.Zhdanov, A.D.Manukhova, T.V.Sharov, Y.V.Kapitonov, Bull.Russ.Acad.Sci. **77** (2013), 935-938
[15] J.Hollenshead, L.Klebanoff, J.Vac.Sci.Technol.B. **24** (2006), 64-82
[16] K.R.Passerba, A.J.Gellman, J.Chem.Phys. **115** (2001), 6737-6751
[17] K.A.Fitchhorn, R.A.Miron, Phys.Rev.Lett. **89** (2002), 196103
[18] T.E.Allen, R.R.Kunz, T.M.Mayer, J.Vac.Sci.Technol.B. **6** (1988), 2057-2060
[19] N.Silvis-Cividjian, C.W.Hagen, L.H.A.Leunissen, P.Kruit, Microel.Eng. **61-62** (2002), 693-699
[20] K.Kanaya, S.Okayama, J.Phys.D. **5** (1972), 43-58
[21] L.Reimer, Scanning Electron Microscopy: Physics of Image Formation and Microanalysis, 2nd-ed., Springer, Berlin, 1998
[22] R.W.Nosker, J.Appl.Phys.**40** (1969), 1872-1882
[23] J.D.Fowlkes, S.J.Randolph, P.D.Rack, J.Vac.Sci.Technol.B. **23** (2005), 2825-2832
[24] K.Rykaczewski, W.B.White, A.G.Fedorov, J.Appl.Phys. **101** (2007), 054307
[25] S.A.Rishton, P.D.Kern, J.Vac.Sci.Technol.B. **5** (1987), 135-141
[26] E.G.Seebauer, C.E.Allen, Prog.Surf.Sci. 49 (1995), 265-330